Title

Effects of Nozzle Geometry on the Fluid Dynamics of Thin Liquid Films Flowing down Vertical Strings in the Rayleigh–Plateau Regime

Journal

Langmuir, 33(25)

ISSN

0743-7463

Authors

Sadeghpour, Abolfazl
Zeng, Zezhi
Ju, Y Sungtaek

Publication Date

2017-06-27

DOI

10.1021/acs.langmuir.7b01277

Peer reviewed

Effects of Nozzle Geometry on the Fluid Dynamics of Thin Liquid Films Flowing down Vertical Strings in the Rayleigh-Plateau Regime

*Abolfazl Sadeghpour, Zezhi Zeng, Y. Sungtaek Ju**

Mechanical and Aerospace Engineering Department, University of California, Los Angeles, 420 Westwood Plaza, Los Angeles, California 90095, United States

KEYWORDS: Rayleigh-Plateau instability, liquid films, high-curvature surface, Nusselt solution

ABSTRACT: Thin-liquid films flowing down vertical strings undergo instability, creating wavy film profiles and traveling beads. Previous studies assumed that the liquid film thickness and velocity profiles within the healing length from a nozzle were specified by the Nusselt solution, independent of the nozzle geometry. As a result, the influence of the nozzle diameter on the flow characteristics, such as the liquid bead size, spacing, and traveling speed, was largely overlooked. We report an experimental and numerical simulation study on liquid-film flows in the Rayleigh-Plateau regime while systematically varying the nozzle diameter from 0.5 mm to 3.2 mm at different mass flow rates (0.02, 0.04, 0.06 and 0.08 g/s). We find that the nozzle diameter does have a strong influence on the flow regime as well as flow characteristics. We identify the thickness of a nearly flat portion of a liquid film that precedes the onset of instability, which we term the pre-instability thickness, as a critical flow parameter that govern the size, spacing, and frequency of liquid beads that develop downstream. By defining the liquid film aspect ratio α in terms of the pre-instability thickness, we capture a flow transition from the

Rayleigh-Plateau (RP) instability regime to the isolated droplet regime. An improved understanding of the flow regimes and characteristics assists a systematic design and optimization of a wide variety of processes and devices, including fiber coating and direct contact heat and mass exchangers.

INTRODUCTION

The characteristics of thin liquid films flowing down vertical strings of diameter of the order of 1 mm has attracted a lot of experimental and theoretical interest due to their significance in fiber coating and direct-contact heat[1,2] and mass exchangers[3,4]. The latter has diverse applications, including dry cooling of thermoelectric power plants, thermally driven absorption/adsorption chillers, thermal energy recovery[5], and vapor or CO_2 capturing[6–9]. Past studies showed that wetted wire columns deliver comparable heat transfer performance at lower air pressure drops than packed beds[10,11]. Rigorous fundamental understanding of liquid film flows is important for physics-based design and optimization of such heat and mass exchangers.

As a liquid film flows down a thin string of high curvatures, interplay among surface tension, viscous diffusion, and inertia leads to flow instability, creating periodic or aperiodic liquid beads traveling along the strings. Rayleigh described the importance of surface tension in wave formation in liquid columns[12]. A comparison between liquid film flows over a planar and a curved surface illustrated the effects of surface curvature on velocity profiles[13]. Trifonov et al.[14] studied the nonlinear wavy regimes of viscous liquid film flows on vertical wires using integral method. Quéré observed the formation of axisymmetric drops when a wire was drawn from a liquid bath and related the liquid bead formation to mean flow advection[15,16]. Kalliadasis et al.[17]showed that for film thicknesses larger than a threshold value, the Rayleigh-Plateau instability triggers natural disturbances of the flow, which then leads to liquid drop formation.

Early theoretical and experimental studies of liquid film flows down vertical wires employed highly viscous liquids and thin fibers to reduce the effects of gravity. They observed the existence of a dominant wavelength and the formation of uniformly-spaced beads[18]. A later study[19] investigated flows under similar conditions and developed a creeping-flow model to predict flow characteristics.

Lin et al.[20] took the gravitational force into account for the stability problem of the free coating of and concluded that any flow in this configuration, regardless of the liquid Reynolds number and string diameter, is unstable. Craster et al.[21] derived an evolution model for liquid film flows under a long-wavelength approximation for the thin-layer limit where the radious of total fluid is much smaller than the capillary lengthscale, whose prediction yielded a good agreement with experimental results. Wehinger et al.[22] conducted a numerical simulation study using the multi-fluid method to capture the sinusoidal and solitary wave limits. Grünig et al.[23] experimentally investigated the fluid dynamics of a single wetted string in the presence of significant counterflowing air and observed a limit for gas load where the beads break up into small droplets and flooding occurs.

Ruyer-Quil et al.[24] developed a two-equation evolution model for liquid film flows that accounted for the effects of viscous diffusion and inertia to predict liquid film profiles as a function of time. This and follow-up studies observed wavy flow regimes, where discrete liquid beads are formed and travel down a string at regular or irregular intervals. Extending these studies, Duprat et al.[25] proposed a flow regime map based on a parameter set including the liquid mass flow rate, liquid properties and string diameter. Flow regimes, which are affected by the effects of viscous dispersion, inertia, flow advection and azimuthal curvature, were classified

into four categories[26]. Duprat et al.[24,25,27] also studied the effects of controlled excitations applied at the liquid inlet reservoir.

Previous studies largely overlooked the effects of nozzle geometry on the characteristics of liquid film flows down vertical strings. One generally considers that a liquid film has a smooth or non-wavy region that extends from the nozzle to the location of the onset of instability. The liquid velocity profile within such a non-wavy region was assumed to be given by the so-called Nusselt solution, which is not a function of axial position and nozzle geometry. This approximation may have been made in part to facilitate obtaining solutions to simplified Navier-Stokes equations. To mitigate challenges in the alignment of strings, experimental studies may also have employed large-diameter nozzles, which may have obscured the effects of nozzle geometry. With a "pre-instability" region prescribed independent of the nozzle, all parameters characterizing liquid flows, including liquid bead frequency and diameter, were considered to be independent of the nozzle radius. Our recent study [11], however, suggested that the nozzle radius does influence liquid-film flow characteristics, including the liquid bead diameter and bead frequency.

In the present manuscript, we report our combined experimental and numerical systematic study of the effects of nozzle geometry on thin liquid films flowing down a vertical string. We limit ourselves to experimental conditions within the Rayleigh-Plateau (RP) instability regime [28]. We experimentally determine how the nozzle radius influences the flow characteristics such as the healing length, liquid bead diameter, liquid bead spacing and liquid bead spatial frequency. To help interpret experimental results, we perform sets of numerical simulations. Previous studies simulated the formation of liquid beads on vertical strings under both flowing and static conditions. Mead-Hunter et al.[29] simulated the breakup of a liquid film on a vertical string using

the OpenFOAM CFD package and achieved good agreement in droplet spacing with theoretical results based on the Quere theory[16]. Hosseini et al.[9] simulated thin liquid film flows using the volume of fluid (VOF) method. Their work could qualitatively capture the experimentally obtained profiles of liquid beads but the predicted liquid bead spacing deviated from experimental results. An approximate analytical model is proposed, which relates the flow characteristics.

FLOW REGIME

Interplay among surface tension, inertia and viscous forces governs liquid film flowing down a vertical string which has the potential to show various patterns such as regular train of drop-like beads or solitary waves (wavelike regime)[25]. Previous studies proposed flow regime maps in terms of the liquid mass flow rate, string diameter and liquid properties [24]. **Figure 1** shows one such regime map based on the normalized string radius R_s/l_c and the film aspect ratio $\alpha_N = h_N/R_s$. Here, R_s is the radius of the string; l_c is the capillary length of the liquid; and h_N is the Nusselt thickness or the thickness of a flat liquid film before the onset of instability. The Nusselt thickness in turn is a function of the liquid mass flow rate and the string radius but is independent of nozzle geometry.

The ratio between the growth time of RP instability, τ_g, and the time needed for the flow to displace its wave over the wavelength, τ_a, defines the saturation number β^*. The saturation number is a function of α_N and R_s/l_c. The curve $\beta^* = 1$ divides the coordinate plane into an inertia-dominated region to its right and a surface tension-dominated region to its left. The curve $\beta^* = 1.507$, obtained from a dispersion analysis on traveling beads, demarks a transition between absolute and convective instability. In convective instability, liquid films exhibit disturbed noise-

driven flows where liquid drops are not uniformly spaced and exhibit coalescence [28]. In this study, we limit ourselves to flows in the RP regime with absolute instability.

One limitation of this flow regime map is its inability to capture the effect of nozzle geometry. Our numerical simulation and experimental results show that cases with the same liquid mass flow rate, string diameter and working liquid can exhibit very different flow regimes (e.g., isolated droplet regime; the convective instability regime; and the Rayleigh-Plateau instability regime) depending on the nozzle diameter (see Figure S1 in Supporting Information).

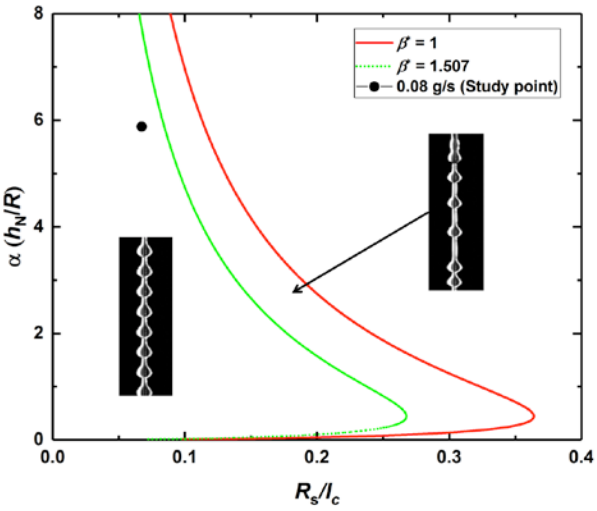

Figure 1. Flow regime map for thin liquid film flows down vertical strings. The symbol represents one flow condition we investigated: silicone oil v50 with a mass flow rate Q = 0.08 g/s on a string of diameter 0.2 mm.

EXPERIMENT AND NUMERICAL SIMULATION

We perform a systematic experimental and numerical study to investigate the influence of nozzle geometry on the flow characteristics such as the healing length, spatial/temporal frequency of traveling beads, and their spacing and size.

EXPERIMENTAL SETUP

Figure 2 shows a schematic of the experimental setup we use to study the effects of nozzle geometry. A syringe pump is used to pump the liquid. The liquid flow rates are varied from 0.02 g/s to 0.09 g/s. A high-speed camera is mounted on an X-Y stage to capture liquid film profiles along vertically mounted Nylon strings. A frame rate of 1000 frame/second is used for all experimental results reported here. A video zoom lens is interchangeably used to capture details of individual liquid beads. The uncertainty in the liquid bead radius and length is estimated to be ± 0.08 mm and that in the liquid bead spacing ± 0.3 mm.

We use stainless steel nozzles of inner diameters varying from 0.5 mm to 3.2 mm and wall thicknesses varying from 0.1 mm to 0.2 mm in our experiments. Nylon strings of length 0.6 m and diameters of 0.2, 0.29 and 0.43 mm are mounted vertically using a weight attached at the end. A set of two X-Y stages are used to align each string such that it is centered with respect to a nozzle. We monitor the liquid mass flow rate using a precision weight scale of resolution 0.1 g with a computer readout.

Rhodorsil silicone oil v50 (density ρ = 963 kg/m^3, kinematic viscosity ν = 50 mm^2/s, surface tension γ = 20.8 mN/m at 20 °C) and Rhodorsil silicone oil v100 (density ρ = 963 kg/m^3, kinematic viscosity ν = 100 mm^2/s, surface tension γ = 20.8 mN/m at 20 °C) are used as the liquids.

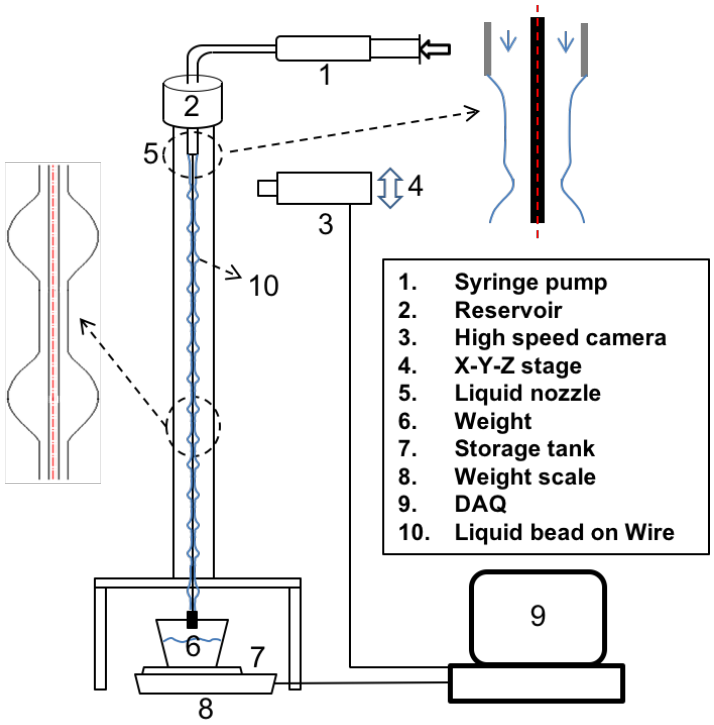

Figure 2. Schematic of the experimental setup.

Using the captured video images, we extract relevant flow parameters, including the liquid bead spacing, the liquid bead temporal frequency, the liquid bead velocity, the healing length, the pre-instability thickness and the liquid bead radius (see Figure S2 in Supporting Information). The first three parameters are determined from a so-called spatiotemporal diagram, which we construct by extracting a single vertical line of pixels that intersect liquid beads near their centers from each of the video frames and then juxtaposing them along the horizontal time axis. The vertical axis represents the distance from the tip of the nozzle. As for the healing length, we consider the onset of instability at the location where local perturbations exceed 4% of the mean liquid film thickness.

NUMERICAL SIMULATION

To help understand experimental results, we perform sets of numerical simulations. **Figure 3** shows the simulation domain and boundary conditions we use. We implement the volume of fluid (VOF) method within the framework of a commercial CFD package (ANSYS-Fluent) to model two-phase flows and track liquid-gas interfaces. We assume that the flows are two-dimensional and axi-symmetric. We employ an unsteady 2D solver utilizing the PISO (pressure implicit with splitting of operators) method to handle the pressure-velocity coupling. The pressure staggering option (PRESTO) is used to handle the pressure and the second-order upwind scheme is used to discretize the momentum equations. A mesh independence study is carried out to ensure that the predicted liquid flow parameters, including the liquid bead spacing and diameter, do not change by more than 2% with a further mesh refinement. An unstructured quadratic mesh with the minimum element size of the order of 0.01 mm and the number of mesh elements of the order of 200,000 is used in typical simulation runs.

We adopt the continuum surface force (CSF) model proposed by Brackbill et al.[30], where the effect of surface tension is represented as a source term in the momentum equations. The apparent contact angle[31] is dynamically calculated based on the equilibrium of forces at each instant[32,33]. We do not employ any artificial perturbation in our simulation but rely instead on noise inherent in numerical simulation to initiate instability.

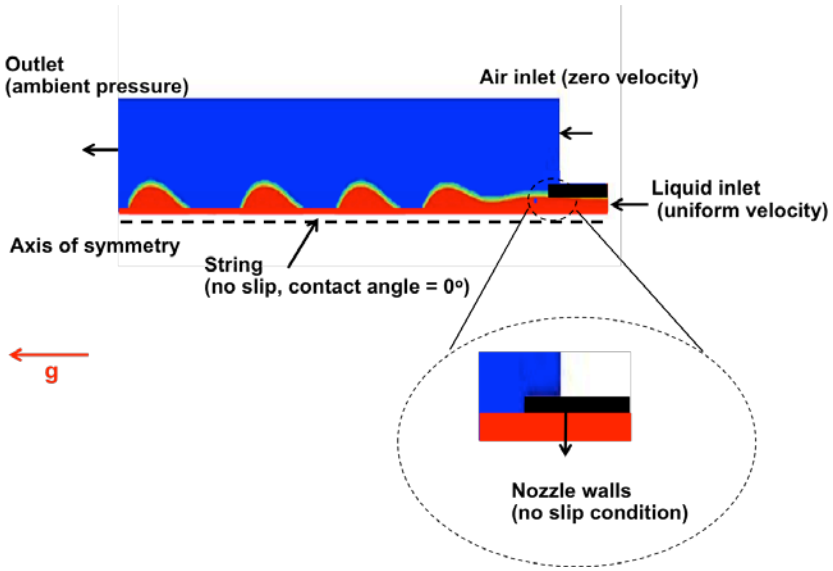

Figure 3. Schematic of boundary conditions for numerical simulation

During a flow initiation stage, liquid beads formed near the nozzle spread and slide down an initially dry string. Our numerical simulation results showing two liquid film profiles: (a) shortly after the beginning of a simulation run and (b) after a steady state has been established (see Figure S3 in Supporting Information). The geometric characteristics of liquid beads, especially bead spacing, during this flow initiation stage differ markedly from those under the later steady state condition We consider that a steady-state has been reached when the spacing between 5 consecutive beads passing a fixed position varies less than 5% of their mean value. All simulation results reported later in the manuscript are obtained after such initiation stage has ended and stable liquid profiles are established.

RESULTS AND DISCUSSION

We first compare the relative effects of two nozzle geometric parameters: nozzle inner diameter (ID) and nozzle outer diameter (OD). **Figure 4** shows the predicted and measured bead temporal frequency as a function of the nozzle inner diameter. For the results shown in **Figure 4**(a), the nozzle wall thickness is varied such that the nozzle OD is fixed. Under this condition, both the simulation and experimental results show that the flow characteristics are relatively insensitive to the nozzle ID. In contrast, the results shown in **Figure 4**(b) are obtained from nozzles with the same ID but different ODs. This time the bead temporal frequency (and other flow parameters) do vary appreciably with the nozzle outer diameter.

The above trend can be explained by considering the profile of a liquid film near the nozzle. The predicted liquid profiles for different values of the liquid contact angle illustrate that, at relatively low contact angles, as is the case for well-wetting silicone oils, the contact line remains attached to the outer nozzle surface (see Figures S4 and S5 in Supporting Information). As a result, the liquid bead diameter and other flow parameters are governed only by the nozzle outer diameter and do not change much with the contact angle. When the contact angle exceeds a threshold value, approximately 45 degrees, the contact line recedes from the outer surface and moves towards the nozzle inner surface. The liquid bead diameter decreases more appreciably with increasing contact angle at these higher contact angles. With these results, we present all subsequent results on flow parameters as a function of the nozzle OD.

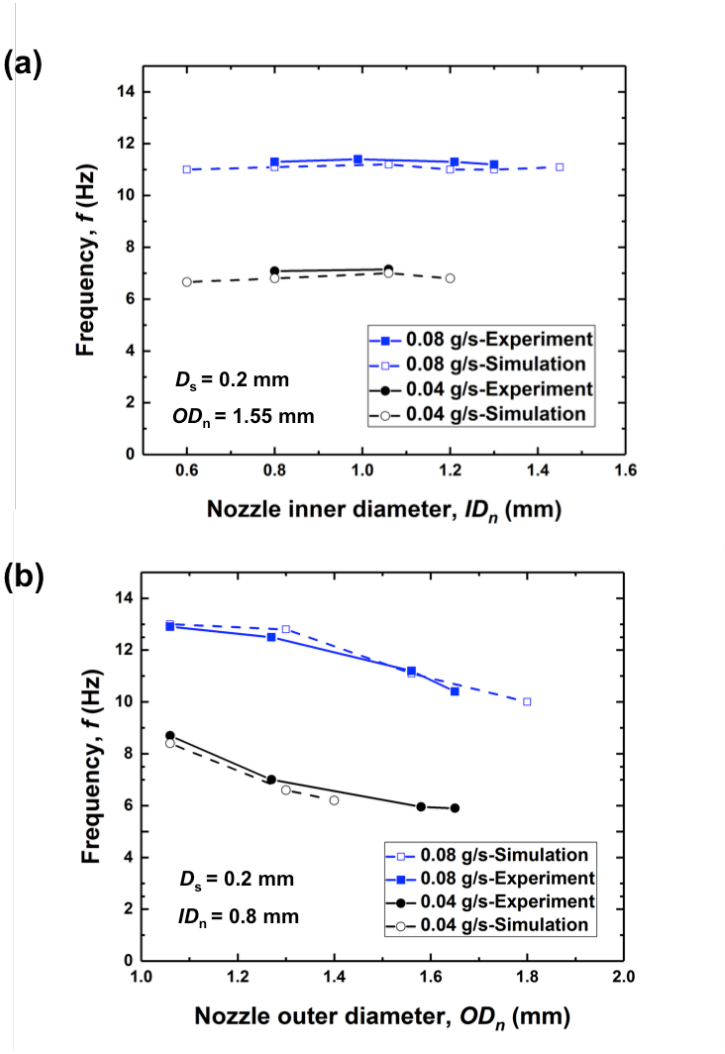

Figure 4. Dependence of the liquid bead frequency on (a) the nozzle inner diameter when the nozzle outer diameter is fixed and (b) the nozzle outer diameter when the nozzle inner diameter is fixed. Two sets of data for two different liquid flow rates (Q = 0.08 g/s and 0.04 g/s) are shown. The hollow symbols correspond to our simulation results and the solid symbols correspond to our experimental results.

Figure 5 and **Figure 6** show two of the flow characteristics for silicone oil v50 flowing down a vertical string with a diameter of 0.2 mm at two different liquid mass flow rates of 0.04 and

0.08 g/s. The liquid bead frequency and the healing length decrease with increasing nozzle outer diameters whereas the bead spacing and the bead diameter increase with increasing nozzle outer diameters (see Figures S6 and S7 in Supporting Information). The predicted results all agree well with the experimentally measured values.

One noteworthy observation is that the flow regime itself can change as we change the nozzle outer diameter. Our experimental and numerical results show that the flows can transition to the isolated droplet regime, as shown in **Figure 5**.b(III), when the nozzle outer diameter is larger than 1.6 mm (for Q = 0.04 g/s) or 2.1 mm (for Q = 0.08 g/s). At even lower liquid mass flow rates (0.025 ~ 0.04 g/s), the flows are observed to be in convective instability regime when the nozzle outer diameter is less than 0.7 mm, which is shown in **Figure 5**.b(I). The previous flow regime map would have predicted all of these flows to be in the absolute instability regime shown in **Figure 5**.b(II).

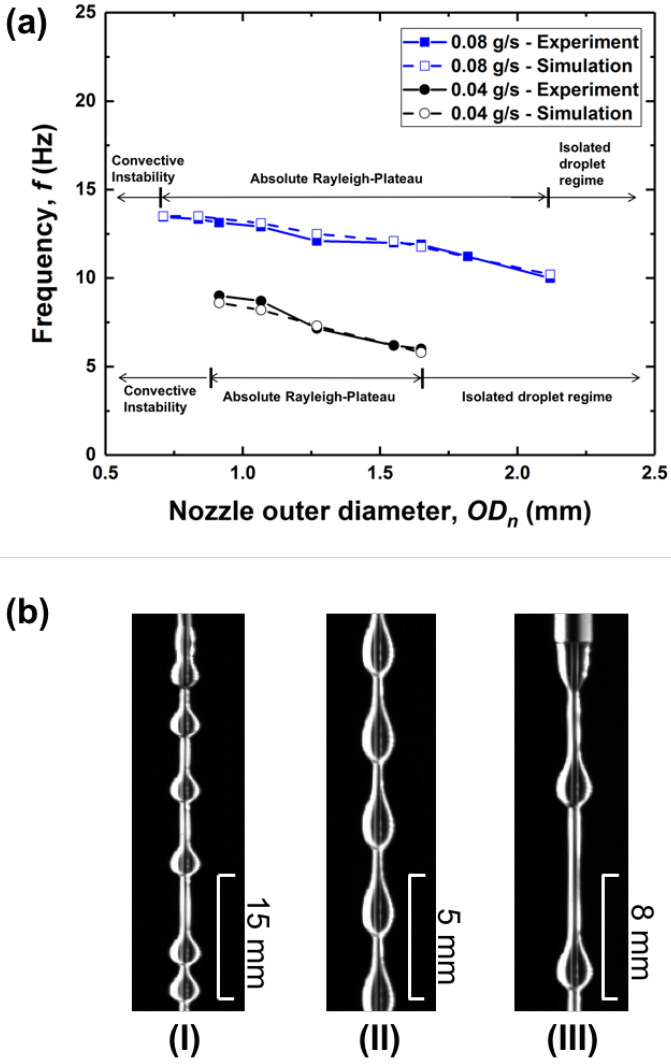

Figure 5. The measured and predicted liquid bead spatial frequency as a function of the nozzle OD for RP regime in (a). Two sets of results are presented for two different mass flow rates: 0.04 and 0.08 g/s. The experimental liquid film profiles are presented for b(I) convective instability, b(II) absolute RP instability and b(III) isolated droplet regimes. Note that the experimental data shown in (a) are only for liquid film flows in the Rayleigh-Plateau regime illustrated in (b-II).

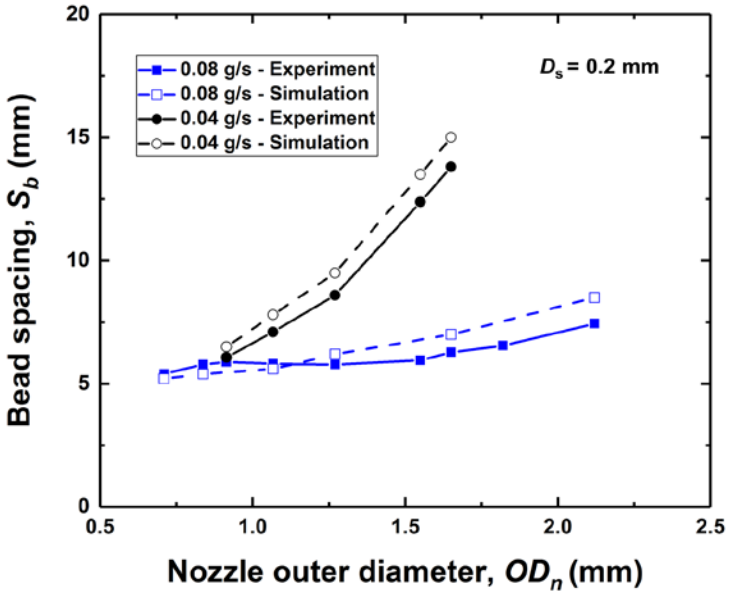

Figure 6. The predicted and measured liquid bead spacing as a function of the nozzle OD. Two sets of results are presented for two different mass flow rates: 0.04 and 0.08 g/s.

We hypothesize that the pre-instability region (between the nozzle and the location of instability onset) is a key to understanding the observed dependence of the flow characteristic parameters on the nozzle outer diameter.

Figure 7(a) shows the predicted liquid film profiles near two nozzles of different diameters. The flows are in the RP regime. As the liquid exits the nozzle, it develops to form (nearly) "flat" liquid-gas interfaces before any flow instability leads to the generation a neck and subsequently discrete liquid beads. We define the thickness of this flat liquid film before the onset of the instability as the pre-instability thickness. **Figure 7**(b) shows the predicted axial velocity profiles in the pre-instability regions at locations marked with the arrows in **Figure 7**(a).

We note that the pre-instability thicknesses and the velocity profiles deviate from the predictions of the Nusselt model despite the fact that the string diameter and the liquid mass flow rate are kept the same for both cases.

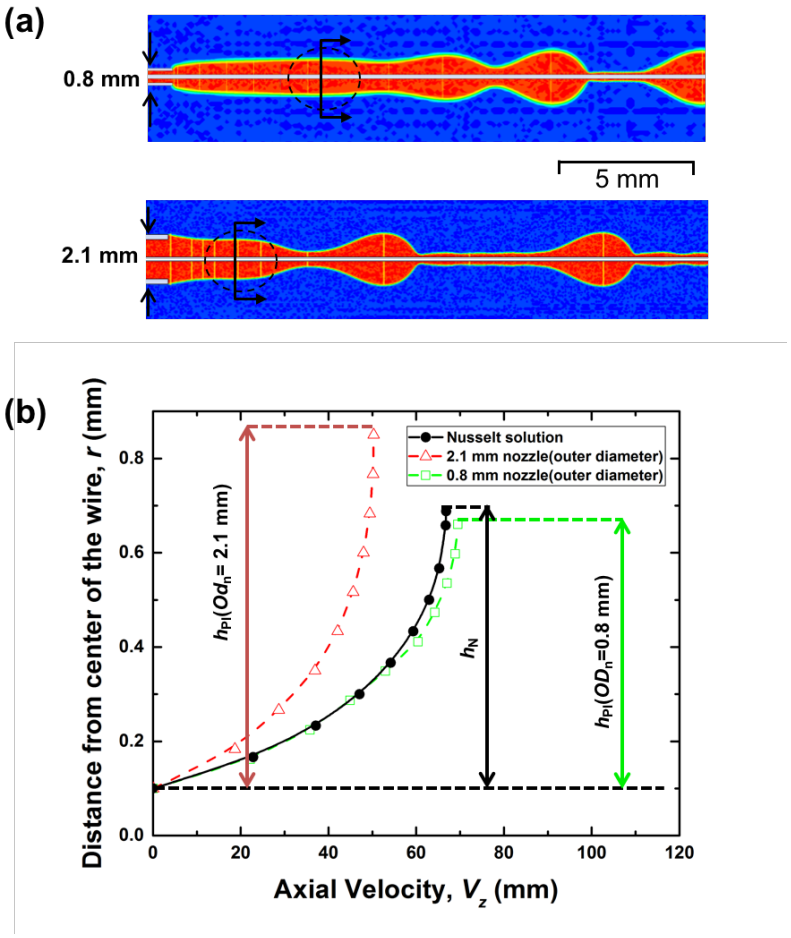

Figure 7. (a) Predicted liquid film profiles near the nozzles for different nozzle outer diameters (2.1 and 0.8 mm). (b) Predicted axial velocity profiles at locations marked with arrows in the pre-instability regions. Note that the horizontal axis corresponds to the axial velocity. The hollow triangles are for OD = 2.1 mm and the hollow squares are for OD = 0.8 mm. The solid line/filled symbols correspond to the Nusselt solution.

We also examine the effect of the nozzle outer diameter on the pre-instability diameter, which is computed as the sum of the string diameter and the pre-instability thickness. We observe that the pre-instability diameter generally increases with increasing nozzle outer diameters or increasing liquid mass flow rates. This simulation results once again agree well with our experimental data (see Figure S8 in Supporting Information).

Figure 8 shows the experimentally measured pre-instability diameter as a function of the nozzle outer diameter in the RP regime using strings with different diameters, different liquids with different viscosities, and different liquid mass flow rates. Once again, we observe that the pre-instability diameter increases with the nozzle outer diameter. At the higher flow rates, the pre-instability diameter approaches a limiting value of approximately 1.65 mm. At the lower liquid flow rates, the pre-instability diameter also increases with increasing nozzle outer diameters but the flows transition into the isolated droplet regime before the pre-instability diameter reaches the limiting value. These trends are observed for both fluids and all the string diameters examined.

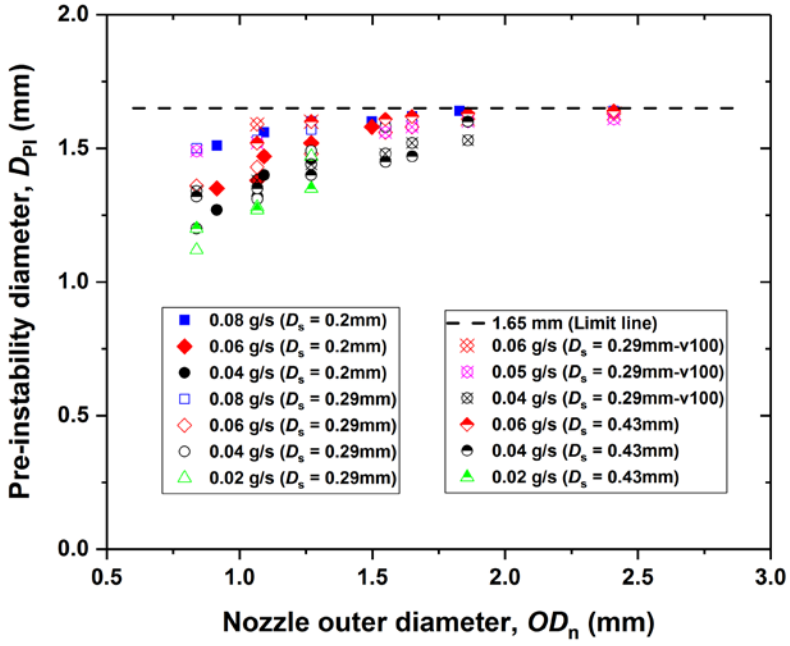

Figure 8. The pre-instability diameter experimentally measured as a function of the nozzle outer diameter. Experiments are performed using two different liquids (silicone oil v50 and v100); three different string diameters (0.2, 0.29 and 0.43 mm); and four different liquid mass flow rates (0.02, 0.04, 0.06, and 0.08 g/s).

The flow regime map reported in previous studies does not have any provision to account for the effects of the nozzle geometry. We propose a modified flow regime map where we attempt to account for the influence of the nozzle outer diameter by replacing the Nusselt thickness with the pre-instability thickness in calculating the liquid film aspect ratio α.

Figure 9(a) shows all of our experimental and numerical simulation conditions on the previous flow regime map. All of our cases would be in the RP regime according to this regime map. **Figure 9**(b) shows our new flow regime map, which can now capture the transition to the isolated droplet regime. The film aspect ratios for flows in the isolated bead regime, where there

is no well-defined pre-instability region, are calculated using "equivalent" pre-instability thickness values using the relation discussed later.

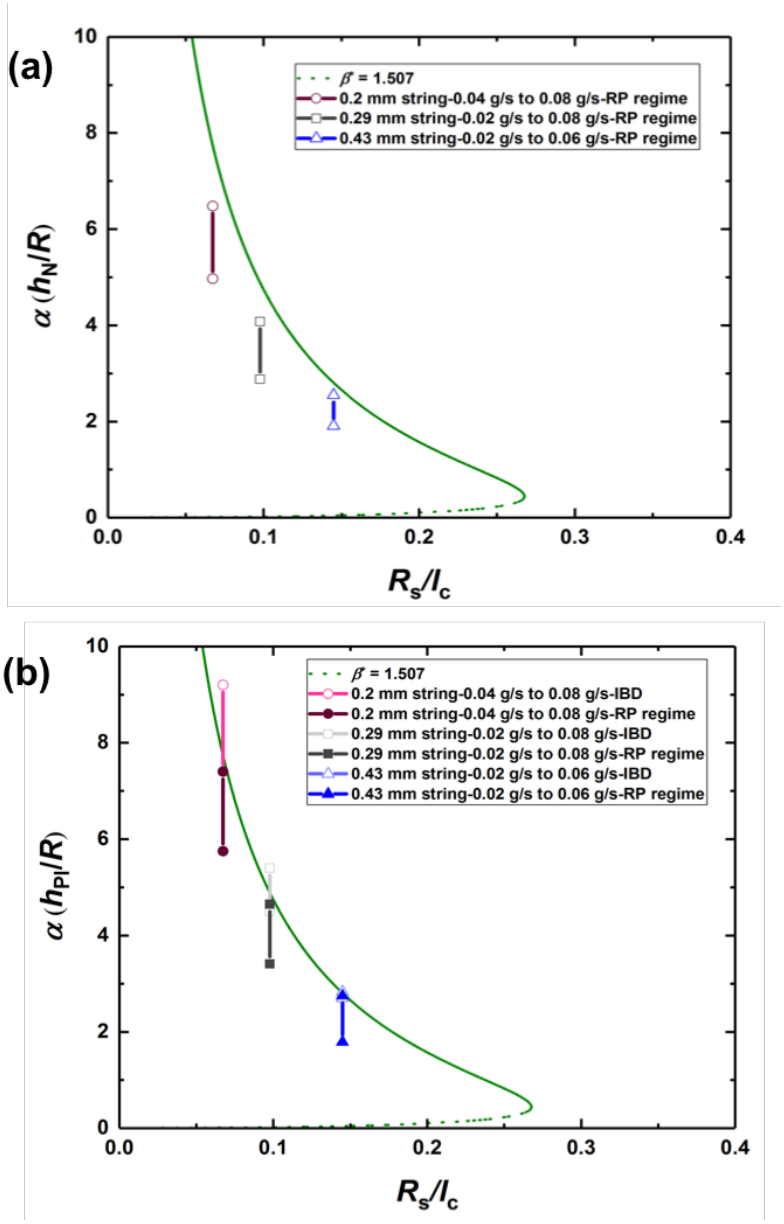

Figure 9. (a) The flow regime map proposed in previous studies. The Nusselt thickness is used to define the liquid film aspect ratio α. (b) The newly proposed flow regime map. The pre-instability thickness is used instead to define α.

We proposed an inter-relationship between the flow parameter. In this method, the bead diameter can be calculated using the pre-instability thickness and the bead velocity and frequency are found by the bead diameter value. The spacing, which is the division of the bead velocity and frequency, then, can be calculated. Based on these inter-relationships and a simplified free body diagram of a liquid bead on a vertical string, we develop semi-empirical models to help calculate the flow parameters from the pre-instability thickness (see Figures S9 and S10 in Supporting Information).

Based on our experimental results, we first develop an empirical correlation between the liquid bead diameter D_b and the pre-instability thickness h_{PI}:

$$D_b/2 = 1.45 \times h_{PI} + D_s/2 \quad (1)$$

Figure 10 shows that the bead diameters calculated using our empirical model agree well with the experimental data. There is an approximately linear relationship between the pre-instability thickness and the liquid bead diameter. As a result, the limiting pre-instability thickness results in a corresponding limit for the bead diameter as illustrated in **Figure 10**.

Next, we model a liquid bead as a rigid object sliding down on a thin liquid substrate. Based on our numerical simulation results, we approximate the velocity of the liquid at the surface of the substrate as half the bead velocity, $V_b/2$, and the liquid substrate thickness as $\frac{h_{PI}}{h_N} \times R_b$. From the force balance, we then derive the following semi-empirical equation for the bead velocity, V_b :

$$V_b = \frac{h_{PI}}{h_N} \times R_s \times \frac{\rho g}{\mu \times (R_s \times (\frac{h_{PI}}{h_N} + 1))} \times \left(\frac{2}{3} R_b^2 - \left(R_s \times (\frac{h_{PI}}{h_N} + 1) \right)^2 \right) \quad (2)$$

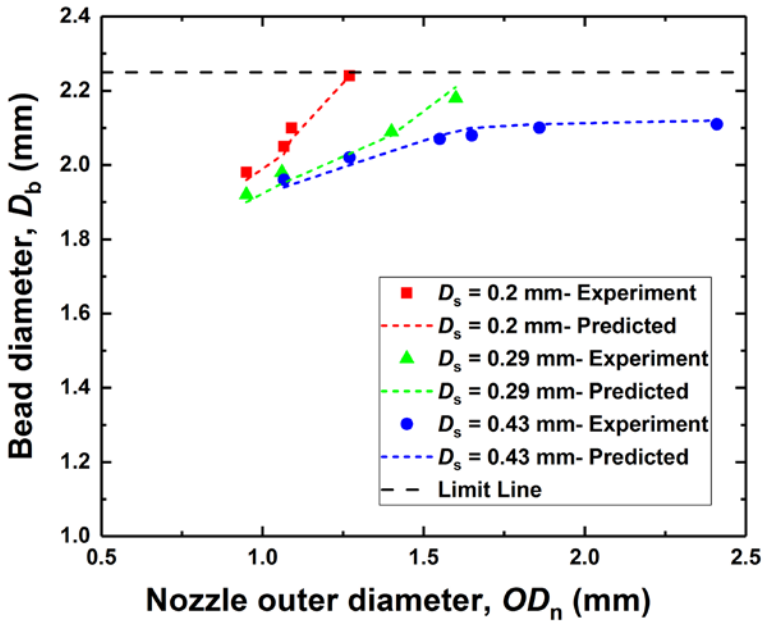

Figure 10. The liquid bead diameter as a function of the nozzle outer diameter. The solid symbols represent the experimental data and the dashed lines correspond to the values calculated from the empirical model. The liquid mass flow rate is 0.06 g/s. The limit line corresponds to the limit line of pre-instability diameter.

The liquid bead velocities calculated from the semi-empirical model agree well with the measured values (see Figure S11 in Supporting Information). We note that, as the pre-instability diameter increases with decreasing string diameters, the bead velocity also increases. This can be explained by the fact that liquid beads formed from thicker pre-instability regions are bigger. Since the bead volume and corresponding gravity force grow faster (~ D_b^3) than the viscous force on the inner side of the sliding bead (~D_b^2), the bead velocity increases with the pre-instability thickness

The bead frequency f can be readily calculated from the mass flow rate and the mass of an individual liquid bead. We first obtain the part of the mass flow rate contributed by liquid beads by subtracting the part of the mass flow rate contributed by the liquid substrate from the total mass flow rate. The liquid bead is assumed to be a sphere of diameter D_b. We then obtain

$$f = \frac{Q}{\rho \times \left(\frac{2}{3}\pi R_b^3 - 2R_b\pi \times (R_s)^2\right)} \quad (3)$$

The liquid bead frequency decreases with increasing pre-instability thicknesses (due to either increasing nozzle outer diameter or decreasing string diameter) because of the corresponding increase in the diameter of liquid beads and hence their mass (see Figure S12 in Supporting Information). The liquid bead frequency needs to decrease to maintain the same liquid flow rate. The bead spacing can be obtained by simply dividing the liquid bead velocity by the bead frequency.

Moreover, as an increase in the bead diameter leads to an increase in the bead velocity and a decrease in the bead frequency to satisfy the mass conservation, the limiting value of the bead diameter translates into a corresponding upper limit for the bead velocity (see Figure S11 in Supporting Information) and a corresponding lower limit for the bead frequency (see Figure S12 in Supporting Information). We emphasize that these limiting values represent limits for liquid film flows to stay in the Rayleigh-Plateau regime and not other physical limits.

Earlier studies[16,34] related the liquid bead spacing to the dominant wavelength for instability, $2\pi\sqrt{2}h$, in cylindrical liquid columns. This result, however, was obtained for static liquid films whose thicknesses are much smaller than the string radius. These conditions do not strictly apply in flowing liquid films considered in the present study. The classical relationship indeed does not directly capture the relationship between the bead spacing and the flow rate ($S_b \sim Q^{-1}$) illustrated,

for example, in **Figure 6**. Our semi-analytical models (Eqs. 2 and 3), however, do suggest that the bead spacing, S_b, is linearly related to the pre-instability thickness, h_{PI}. Comparing bead spacing results in **Figure 6** and the corresponding pre-instability diameters, we also generally note an approximately linear dependence of the bead spacing on the pre-instability diameter (see Figure S8 in Supporting Information).

CONCLUSION

We report our experimental and numerical simulation study on the effects of nozzle geometry on the characteristics of thin liquid films flowing down vertical strings with diameters of 0.2, 0.29 and 0.43 mm under the ranges of liquid flow rates (0.02, 0.04, 0.06 and 0.08 g/s) where the Rayleigh-Plateau instability is the dominant instability mechanism. The nozzle inner diameters are varied from 0.5 to 3.2 mm. We identify that the portion of a liquid film near the nozzle, which precedes the onset of the instability, as a key to the down-stream flow characteristics, such as the liquid bead size, spacing, and traveling speed. The thickness of a nearly flat part of this pre-instability region is termed the pre-instability thickness, which differs from the Nusselt thickness often presumed in the literature. We show that an increase in the nozzle diameter at a fixed mass flow rate leads to an increase in the pre-instability thickness. This in turn results in increases in the liquid bead size, spacing, and traveling velocity. With an increase in the liquid mass flow rate, a decrease in the string diameter, or an increase in the liquid viscosity, the pre-instability thickness grows, approaching a limit before the film flow transition into a different flow regime. This transition is captured in a modified flow regime map where we replace the Nusselt thickness with the pre-instability thickness to define the film aspect ratio. Semi-

empirical models are also developed for the liquid bead size, spacing, and traveling speed as a function of the pre-instability thickness.

ASSOCIATED CONTENT

Supporting Information

Nomenclature.

Figures S1-S12.

AUTHOR INFORMATION

Corresponding Author

*E-mail: just@seas.ucla.edu (Y.S.J.).

Notes

The authors declare no competing financial interest.

ACKNOWLEDGMENT

The present manuscript is based in part on work performed with support from the US National Science Foundation through grant CBET-1358034.

REFERENCES

(1) Zeng, Z.; Warrier, G.; Ju, Y. S. Study of the Fluid Dynamics of Thin Liquid Films Flowing Down a Vertical String With Counterflow of Gas. **2015**, V08BT10A054.

(2) Hattori, K.; Ishikawa, M.; Mori, Y. H. Strings of Liquid Beads for Gas-Liquid Contact Operations. *AIChE J.* **1994**, *40* (12), 1983–1992.

(3) Chinju, H.; Uchiyama, K.; Mori, Y. H. "String-of-Beads" Flow of Liquids on Vertical Wires for Gas Absorption. *AIChE J.* **2000**, *46* (5), 937–945.

(4) Grünig, J.; Lyagin, E.; Horn, S.; Skale, T.; Kraume, M. Mass Transfer Characteristics of Liquid Films Flowing down a Vertical Wire in a Counter Current Gas Flow. *Chem. Eng. Sci.* **2012**, *69* (1), 329–339.

(5) Nozaki, T.; Kaji, N.; Mod, Y. H. Heat Transfer to a Liquid Flowing Down Vertical Wires Hanging in a Hot Gas Stream: An Experimental Study of a New Means of Thermal Energy Recovery. *HEAT Transf.* **1998**, *6*, 63–68.

(6) Uchiyama, K.; Migita, H.; Ohmura, R.; Mori, Y. H. Gas Absorption into "string-of-Beads" Liquid Flow with Chemical Reaction: Application to Carbon Dioxide Separation. *Int. J. Heat Mass Transf.* **2003**, *46* (3), 457–468.

(7) Migita, H.; Soga, K.; Mori, Y. H. Gas Absorption in a Wetted-Wire Column. *AIChE J.* **2005**, *51* (8), 2190–2198.

(8) Pakdehi, S. G.; Taheri, S. Separation of Hydrazine from Air by Wetted Wire Column. *Chem. Eng. Technol.* **2010**, *33* (10), 1687–1694.

(9) Hosseini, S. M.; Alizadeh, R.; Fatehifar, E.; Alizadehdakhel, A. Simulation of Gas Absorption into String-of-Beads Liquid Flow with Chemical Reaction. *Heat Mass Transf.* **2014**, *50* (10), 1393–1403.

(10) Zeng, Z.; Warrier, G.; Ju, Y. S. Flow and Heat Transfer in Liquid Films Flowing Over Highly Curved Surfaces. **2015**, V002T06A012.

(11) Zeng, Z.; Sadeghpour, A.; Warrier, G.; Ju, Y. S. Experimental Study of Heat Transfer between Thin Liquid Films Flowing down a Vertical String in the Rayleigh-Plateau Instability Regime and a Counterflowing Gas Stream. *Int. J. Heat Mass Transf.* **2017**, *108, Part A*, 830–840.

(12) Strutt, J. W.; Rayleigh, Lord. On the Instability of Jets. *Proc Lond. Math Soc* **1878**, *10* (4).

(13) Grabbert, G.; Wünsch, G. Zur Hydraulik Stark Gekrümmter Rieselfilme. *Freib. Forschungshefte A* **1973**, *517*, 61–83.

(14) Trifonov, Y. Y. Steady-State Traveling Waves on the Surface of a Viscous Liquid Film Falling down on Vertical Wires and Tubes. *AIChE J.* **1992**, *38* (6), 821–834.

(15) Quéré, D. Thin Films Flowing on Vertical Fibers. *EPL Europhys. Lett.* **1990**, *13* (8), 721.

(16) Quéré, D. Fluid Coating on a Fiber. *Annu. Rev. Fluid Mech.* **1999**, *31* (1), 347–384.

(17) Kalliadasis, S.; Chang, H.-C. Drop Formation during Coating of Vertical Fibres. *J. Fluid Mech.* **1994**, *261*, 135–168.

(18) Goren, S. L. The Instability of an Annular Thread of Fluid. *J. Fluid Mech.* **1962**, *12* (2), 309–319.

(19) Kliakhandler, I. L.; Davis, S. H.; Bankoff, S. G. Viscous Beads on Vertical Fibre. *J. Fluid Mech.* **2001**, *429*, 381–390.

(20) Lin, S. P.; Liu, W. C. Instability of Film Coating of Wires and Tubes. *AIChE J.* **1975**, *21* (4), 775–782.

(21) Craster, R. V.; Matar, O. K. On Viscous Beads Flowing down a Vertical Fibre. *J. Fluid Mech.* **2006**, *553*, 85–105.
(22) Wehinger, G. D.; Peeters, J.; Muzaferija, S.; Eppinger, T.; Kraume, M. Numerical Simulation of Vertical Liquid-Film Wave Dynamics. *Chem. Eng. Sci.* **2013**, *104*, 934–944.
(23) Grünig, J.; Skale, T.; Kraume, M. Liquid Flow on a Vertical Wire in a Countercurrent Gas Flow. *Chem. Eng. J.* **2010**, *164* (1), 121–131.
(24) Ruyer-Quil, C.; Treveleyan, P.; Giorgiutti-Dauphiné, F.; Duprat, C.; Kalliadasis, S. Modelling Film Flows down a Fibre. *J. Fluid Mech.* **2008**, *603*, 431–462.
(25) Duprat, C.; Ruyer-Quil, C.; Giorgiutti-Dauphiné, F. Spatial Evolution of a Film Flowing down a Fiber. *Phys. Fluids 1994-Present* **2009**, *21* (4), 42109.
(26) Ruyer-Quil, C.; Kalliadasis, S. Wavy Regimes of Film Flow down a Fiber. *Phys. Rev. E* **2012**, *85* (4), 46302.
(27) Duprat, C.; Ruyer-Quil, C.; Giorgiutti-Dauphiné, F. Experimental Study of the Instability of a Film Flowing down a Vertical Fiber. *Eur. Phys. J. Spec. Top.* **2009**, *166* (1), 63–66.
(28) Duprat, C.; Ruyer-Quil, C.; Kalliadasis, S.; Giorgiutti-Dauphiné, F. Absolute and Convective Instabilities of a Viscous Film Flowing Down a Vertical Fiber. *Phys. Rev. Lett.* **2007**, *98* (24), 244502.
(29) Mead-Hunter, R.; King, A. J. C.; Mullins, B. J. Plateau Rayleigh Instability Simulation. *Langmuir* **2012**, *28* (17), 6731–6735.
(30) Brackbill, J. U.; Kothe, D. B.; Zemach, C. A Continuum Method for Modeling Surface Tension. *J. Comput. Phys.* **1992**, *100* (2), 335–354.
(31) Blake, T. D. The Physics of Moving Wetting Lines. *J. Colloid Interface Sci.* **2006**, *299* (1), 1–13.
(32) Hirt, C. W.; Nichols, B. D. Volume of Fluid (VOF) Method for the Dynamics of Free Boundaries. *J. Comput. Phys.* **1981**, *39* (1), 201–225.
(33) Kazemzadeh, A.; Ganesan, P.; Ibrahim, F.; He, S.; Madou, M. J. The Effect of Contact Angles and Capillary Dimensions on the Burst Frequency of Super Hydrophilic and Hydrophilic Centrifugal Microfluidic Platforms, a CFD Study. *PLoS ONE* **2013**, *8* (9).
(34) R.S, L. R. S. XVI. On the Instability of a Cylinder of Viscous Liquid under Capillary Force. *Philos. Mag. Ser. 5* **1892**, *34* (207), 145–154.

For Table of Contents Only